

# $2\nu\beta\beta$ decay of $^{76}\text{Ge}$ into excited states with GERDA Phase I

GERDA Collaboration<sup>‡</sup>

M. Agostini<sup>15</sup>, M. Allardt<sup>4</sup>, A.M. Bakalyarov<sup>13</sup>, M. Balata<sup>1</sup>,  
 I. Barabanov<sup>11</sup>, N. Barros<sup>4§</sup>, L. Baudis<sup>19</sup>, C. Bauer<sup>7</sup>,  
 N. Becerici-Schmidt<sup>14</sup>, E. Bellotti<sup>8,9</sup>, S. Belogurov<sup>12,11</sup>,  
 S.T. Belyaev<sup>13</sup>, G. Benato<sup>19</sup>, A. Bettini<sup>16,17</sup>, L. Bezrukov<sup>11</sup>,  
 T. Bode<sup>15</sup>, D. Borowicz<sup>3,5</sup>, V. Brudanin<sup>5</sup>, R. Brugnera<sup>16,17</sup>,  
 D. Budjáš<sup>15</sup>, A. Caldwell<sup>14</sup>, C. Cattadori<sup>9</sup>, A. Chernogorov<sup>12</sup>,  
 V. D'Andrea<sup>1</sup>, E.V. Demidova<sup>12</sup>, A. di Vacri<sup>1</sup>, A. Domula<sup>4</sup>,  
 E. Doroshkevich<sup>11</sup>, V. Egorov<sup>5</sup>, R. Falkenstein<sup>18</sup>, O. Fedorova<sup>11</sup>,  
 K. Freund<sup>18</sup>, N. Frodyma<sup>3</sup>, A. Gangapshev<sup>11,7</sup>,  
 A. Garfagnini<sup>16,17</sup>, C. Gooch<sup>14</sup>, P. Grabmayr<sup>18</sup>, V. Gurentsov<sup>11</sup>,  
 K. Gusev<sup>13,5,15</sup>, A. Hegai<sup>18</sup>, M. Heisel<sup>7</sup>, S. Hemmer<sup>16,17</sup>,  
 G. Heusser<sup>7</sup>, W. Hofmann<sup>7</sup>, M. Hult<sup>6</sup>, L.V. Inzhechik<sup>11||</sup>,  
 J. Janicskó Csáthy<sup>15</sup>, J. Jochum<sup>18</sup>, M. Junker<sup>1</sup>, V. Kazalov<sup>11</sup>,  
 T. Kihm<sup>7</sup>, I.V. Kirpichnikov<sup>12</sup>, A. Kirsch<sup>7</sup>, A. Klimenko<sup>7,5¶</sup>,  
 K.T. Knöpfle<sup>7</sup>, O. Kochetov<sup>5</sup>, V.N. Kornoukhov<sup>12,11</sup>,  
 V.V. Kuzminov<sup>11</sup>, M. Laubenstein<sup>1</sup>, A. Lazzaro<sup>15</sup>,  
 V.I. Lebedev<sup>13</sup>, B. Lehnert<sup>4</sup>, H.Y. Liao<sup>14</sup>, M. Lindner<sup>7</sup>,  
 I. Lippi<sup>17</sup>, A. Lubashevskiy<sup>7,5</sup>, B. Lubsandorzhiev<sup>11</sup>, G. Lutter<sup>6</sup>,  
 C. Macolino<sup>1</sup>, B. Majorovits<sup>14</sup>, W. Maneschg<sup>7</sup>,  
 E. Medinaceli<sup>16,17</sup>, Y. Mi<sup>18</sup>, M. Misiaszek<sup>3</sup>, P. Moseev<sup>11</sup>,  
 I. Nemchenok<sup>5</sup>, D. Palioselitis<sup>14</sup>, K. Panas<sup>3</sup>, L. Pandola<sup>2</sup>,  
 K. Pelczar<sup>3</sup>, A. Pullia<sup>10</sup>, S. Riboldi<sup>10</sup>, N. Rumyantseva<sup>5</sup>,  
 C. Sada<sup>16,17</sup>, M. Salathe<sup>7</sup>, C. Schmitt<sup>18</sup>, B. Schneider<sup>4</sup>,  
 J. Schreiner<sup>7</sup>, O. Schulz<sup>14</sup>, B. Schwingenheuer<sup>7</sup>, S. Schönert<sup>15</sup>,  
 A-K. Schütz<sup>18</sup>, O. Selivanenko<sup>11</sup>, M. Shirchenko<sup>13,5</sup>, H. Simgen<sup>7</sup>,  
 A. Smolnikov<sup>7</sup>, L. Stanco<sup>17</sup>, M. Stepaniuk<sup>7</sup>, C.A. Ur<sup>17</sup>,  
 L. Vanhoefer<sup>14</sup>, A.A. Vasenko<sup>12</sup>, A. Veresnikova<sup>11</sup>, K. von  
 Sturm<sup>16,17</sup>, V. Wagner<sup>7</sup>, M. Walter<sup>19</sup>, A. Wegmann<sup>7</sup>,

<sup>‡</sup> LNGS, Assergi, Italy; correspondence: gerda-eb@mpi-hd.mpg.de

<sup>§</sup> present address: Dept. of Physics and Astronomy, Univ. of Pennsylvania, Philadelphia, Pennsylvania, USA

<sup>||</sup> also at: Moscow Inst. of Physics and Technology, Russia

<sup>¶</sup> also at: Int. Univ. for Nature, Society and Man “Dubna”, Dubna, Russia

**T. Wester<sup>4</sup>, H. Wilsenach<sup>4</sup>, M. Wojcik<sup>3</sup>, E. Yanovich<sup>11</sup>,  
P. Zavarise<sup>1</sup>, I. Zhitnikov<sup>5</sup>, S.V. Zhukov<sup>13</sup>, D. Zinatulina<sup>5</sup>,  
K. Zuber<sup>4</sup>, and G. Zuzel<sup>3</sup>.**

<sup>1</sup> INFN Laboratori Nazionali del Gran Sasso and Gran Sasso Science Institute, Assergi, Italy

<sup>2</sup> INFN Laboratori Nazionali del Sud, Catania, Italy

<sup>3</sup> Institute of Physics, Jagiellonian University, Cracow, Poland

<sup>4</sup> Institut für Kern- und Teilchenphysik, Technische Universität Dresden, Dresden, Germany

<sup>5</sup> Joint Institute for Nuclear Research, Dubna, Russia

<sup>6</sup> Institute for Reference Materials and Measurements, Geel, Belgium

<sup>7</sup> Max-Planck-Institut für Kernphysik, Heidelberg, Germany

<sup>8</sup> Dipartimento di Fisica, Università Milano Bicocca, Milano, Italy

<sup>9</sup> INFN Milano Bicocca, Milano, Italy

<sup>10</sup> Dipartimento di Fisica, Università degli Studi di Milano e INFN Milano, Milano, Italy

<sup>11</sup> Institute for Nuclear Research of the Russian Academy of Sciences, Moscow, Russia

<sup>12</sup> Institute for Theoretical and Experimental Physics, Moscow, Russia

<sup>13</sup> National Research Centre “Kurchatov Institute”, Moscow, Russia

<sup>14</sup> Max-Planck-Institut für Physik, München, Germany

<sup>15</sup> Physik Department and Excellence Cluster Universe, Technische Universität München, Germany

<sup>16</sup> Dipartimento di Fisica e Astronomia dell'Università di Padova, Padova, Italy

<sup>17</sup> INFN Padova, Padova, Italy

<sup>18</sup> Physikalisches Institut, Eberhard Karls Universität Tübingen, Tübingen, Germany

<sup>19</sup> Physik Institut der Universität Zürich, Zürich, Switzerland

**Abstract.** Two neutrino double beta decay of  $^{76}\text{Ge}$  to excited states of  $^{76}\text{Se}$  has been studied using data from Phase I of the GERDA experiment. An array composed of up to 14 germanium detectors including detectors that have been isotopically enriched in  $^{76}\text{Ge}$  was deployed in liquid argon. The analysis of various possible transitions to excited final states is based on coincidence events between pairs of detectors where a de-excitation  $\gamma$  ray is detected in one detector and the two electrons in the other.

No signal has been observed and an event counting profile likelihood analysis has been used to determine Frequentist 90% C.L. bounds for three transitions:  $0_{\text{g.s.}}^+ - 2_1^+$ :  $T_{1/2}^{2\nu} > 1.6 \cdot 10^{23}$  yr,  $0_{\text{g.s.}}^+ - 0_1^+$ :  $T_{1/2}^{2\nu} > 3.7 \cdot 10^{23}$  yr and  $0_{\text{g.s.}}^+ - 2_2^+$ :  $T_{1/2}^{2\nu} > 2.3 \cdot 10^{23}$  yr. These bounds are more than two orders of magnitude larger than those reported previously. Bayesian 90% credibility bounds were extracted and used to exclude several models for the  $0_{\text{g.s.}}^+ - 0_1^+$  transition.

PACS numbers: 23.40.-s, 21.10.Tg, 27.50.+e, 29.40.Wk

*Keywords:* double beta decay,  $^{76}\text{Ge}$ (enriched), decay to excited states of  $^{76}\text{Se}$ .

Submitted to: *J. Phys. G: Nucl. Phys.*

## 1. Introduction

The observation of neutrinoless double beta ( $0\nu\beta\beta$ ) decay would imply physics beyond the Standard Model of particle physics because the process manifests lepton number violation. Assuming light neutrino exchange as the dominant process, the experimentally observable half-life would be connected to the effective Majorana neutrino mass via a phase space factor ( $F$ ) and a nuclear matrix element (NME,  $\mathcal{M}$ ). Calculations of  $\mathcal{M}$  depend strongly on the nuclear structure model chosen. Uncertainties in the model translate to uncertainties when converting a measured half-life into the Majorana neutrino mass or its limit respectively [1].

Two neutrino double beta ( $2\nu\beta\beta$ ) decay is a weak second order Standard Model process which has been observed in eleven nuclides and double neutrino electron capture ( $2\nu\text{ECEC}$ ) in two nuclides with half-lives between  $T_{1/2}^{2\nu}=10^{18} - 10^{24}$  yr [2, 3]. Due to the different reaction mechanisms the effective Majorana neutrino mass  $\langle m_{\beta\beta} \rangle$  enters only in the half-life for the  $0\nu\beta\beta$  mode, and not for the  $2\nu\beta\beta$  mode:

$$2\nu\beta\beta : \quad (T_{1/2}^{2\nu})^{-1} = F^{2\nu} \cdot |\mathcal{M}^{2\nu}|^2 \quad (1)$$

$$0\nu\beta\beta : \quad (T_{1/2}^{0\nu})^{-1} = F^{0\nu} \cdot |\mathcal{M}^{0\nu}|^2 \cdot \langle m_{\beta\beta} \rangle^2 \quad (2)$$

The NME for  $2\nu\beta\beta$  and  $0\nu\beta\beta$  ( $\mathcal{M}^{2\nu}$ ,  $\mathcal{M}^{0\nu}$ ) and the respective phase space factors ( $F^{2\nu}$ ,  $F^{0\nu}$ ) are numerically different but rely on similar model assumptions. Experimentally verifying the calculations of Eq. (1) reduces to some extend uncertainties of calculations of  $\mathcal{M}^{0\nu}$ . For a recent review see Ref. [4].

Apart from decays into the ground state (g.s.), double beta decays can also occur into excited states of the daughter nucleus. These decay modes are expected to have a lower rate due to a smaller phase space. However, their experimental signature is enhanced by the accompanying de-excitation  $\gamma$  rays. Excited state transitions can in principle occur in both the  $2\nu\beta\beta$  and the  $0\nu\beta\beta$  mode distinguishable only in the different sum of residual electron energies. These investigations provide additional information on the nuclear structure models and more experimental constraints on the system of Eqs. (1 and 2). So far only transitions to the first excited  $0_1^+$  state have been observed, first for  $^{100}\text{Mo}$  [5] in 1995 and for  $^{150}\text{Nd}$  [6] in 2004. Recent half-life values are  $T_{1/2}^{2\nu} = (7.5 \pm 1.2) \cdot 10^{20}$  yr [7] and  $T_{1/2}^{2\nu} = (1.33_{-0.36}^{+0.63}) \cdot 10^{20}$  yr [8], respectively.

The double beta decay of  $^{76}\text{Ge}$  to the ground state of  $^{76}\text{Se}$  has a Q-value of  $Q_{\beta\beta} = (2039.061 \pm 0.007)$  keV [9] and can potentially feed any  $0^+$  or  $2^+$  excited state in  $^{76}\text{Se}$  up to this energy. The search in this work focuses on the  $2\nu\beta\beta$  transitions from the ground state  $0_{\text{g.s.}}^+$  of  $^{76}\text{Ge}$  to the three lowest excited states in  $^{76}\text{Se}$ :  $2_1^+$ ,  $0_1^+$ , and  $2_2^+$  (see Fig. 1). The phase spaces of  $2\nu\beta\beta$  transitions scale with the total available energy  $E$  as  $F^{2\nu} \sim E^{11}$  and reduce the rates for higher energetic states. The rate is further suppressed by the spin-constraint for  $2^+$  states. For the investigated transitions the existing experimental upper limits for half-lives are shown in Table 1. In addition results from theoretical calculations based on various nuclear structure models are presented.

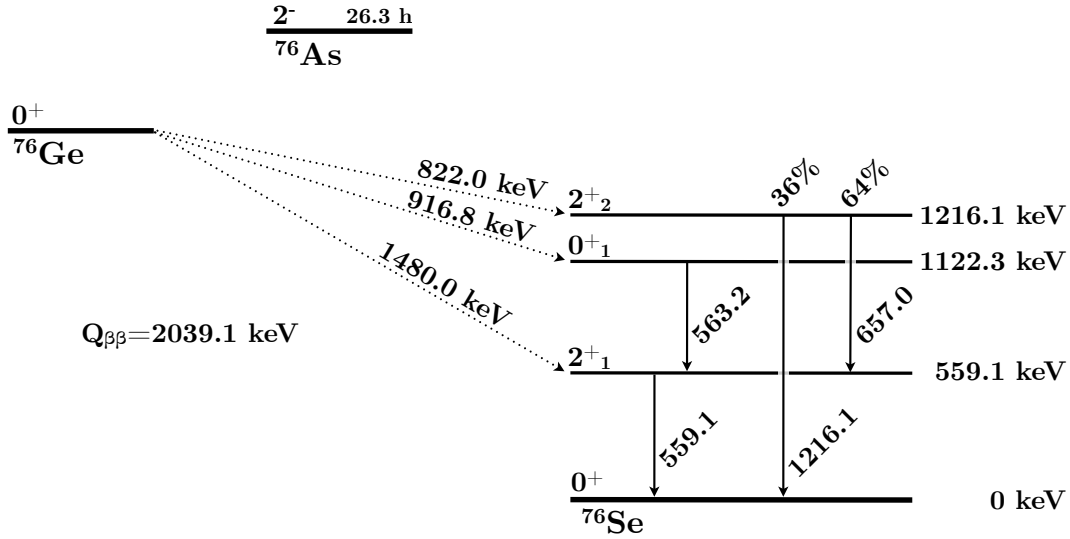


**Figure 1.** Possible double beta decay modes of  $^{76}\text{Ge}$  to excited states of  $^{76}\text{Se}$  that are investigated in this work.

The largest rate is expected for the  $0_{\text{g.s.}}^+ - 0_1^+$  transition and lies within the experimental sensitivity of this analysis. Three calculations have been recently performed for this transition. One is based on the renormalized proton-neutron QRPA using wave functions from Ref. [10]. This calculation predicts a half-life of  $T_{1/2}^{2\nu}(0_1^+) = (1.2 - 5.8) \cdot 10^{23}$  yr for axial vector couplings of  $g_A = 1.26 - 1.00$  [11]. Employing a microscopic interacting boson model (IBM-2), the half-life ratio between the  $0_{\text{g.s.}}^+ - 0_1^+$  and the ground state transition  $0_{\text{g.s.}}^+ - 0_{\text{g.s.}}^+$  is calculated with NMEs and phase space factors from Refs. [12, 13]. The predicted half-life ratio is 3300 for  $^{76}\text{Ge}$  [14]. Scaling this ratio with our recently measured ground state half-life of  $T_{1/2}^{2\nu}(0_{\text{g.s.}}^+) = (1.926 \pm 0.095) \cdot 10^{21}$  yr [15] results in the predicted excited state half-life  $T_{1/2}^{2\nu}(0_1^+) = 6.4 \cdot 10^{24}$  yr independent of  $g_A$ . A shell model (SM) calculation predicts  $T_{1/2}^{2\nu}(0_1^+) = (2.3 - 6.7) \cdot 10^{24}$  yr [16] assuming  $g_A = 1.26 - 1.00$ . The range of  $T_{1/2}^{2\nu}(0_1^+)$  additionally encompasses results of two different effective interactions that have been used also in Refs. [17] and [18]. The SM calculation of  $T_{1/2}^{2\nu}(0_1^+)$  to the ground state is in good agreement with the experimental data. The IBM-2 and SM predictions are significantly longer than other calculations. The current status for the experimental and theoretical situation is summarized in Table 1 for all investigated transitions.

## 2. The coincidence analysis of Gerda Phase I data

The  $\gamma$  cascade following excited state transitions provides a well defined experimental signature which enables large background suppression. The granular installation of the GERDA setup is used to measure coincidences between two germanium detectors. In the following the two detectors are distinguished between (1) a “source” detector where the  $2\nu\beta\beta$  decay occurs and the two electrons are detected and (2) a “gamma” detector

**Table 1.** Experimental half-life limits are compared to model predictions for  $2\nu\beta\beta$  excited state decay modes in  $^{76}\text{Ge}$  as discussed in this paper. The energy of the final level is given. Abbreviations denote: HFB: Hartree-Fock-Bogoliubov, QRPA: Quasi Random Phase Approximation, MCM-QRPA: Multiple Commutator Model QRPA, RQRPA: Renormalized proton-neutron QRPA, IBM: Interactive Boson Model, SM: Shell Model.

$2\nu\beta\beta$ decay mode	$T_{1/2}^{2\nu}$ [yr]	model/exp.	ref.	year
$0_{\text{g.s.}}^+ - 2_1^+$ (559.1 keV)	$> 6.3 \cdot 10^{20}$ (68 % C.L.)	exp.	[19]	1992
	$> 1.1 \cdot 10^{21}$ (90 % C.L.)	exp.	[20]	1995
	$1.2 \cdot 10^{30}$	SM	[21]	1984
	$5.8 \cdot 10^{23}$	HFB	[22]	1994
	$5.0 \cdot 10^{26}$	QRPA	[23]	1994
	$2.4 \cdot 10^{24}$	QRPA	[24]	1996
	$7.8 \cdot 10^{25}$	MCM-QRPA	[25]	1996
	$1.0 \cdot 10^{26}$	RQRPA	[26]	1997
	$(2.4 - 4.3) \cdot 10^{26}$	RQRPA	[27]	1998
	$2.0 \cdot 10^{27}$	RQRPA	[28]	2014
$0_{\text{g.s.}}^+ - 0_1^+$ (1122.3 keV)	$> 6.3 \cdot 10^{20}$ (68 % C.L.)	exp.	[19]	1992
	$> 1.7 \cdot 10^{21}$ (90 % C.L.)	exp.	[20]	1995
	$> 6.2 \cdot 10^{21}$ (90 % C.L.)	exp.	[29]	2000
	$1.32 \cdot 10^{21}$	HFB	[22]	1994
	$4.0 \cdot 10^{22}$	QRPA	[23]	1994
	$4.5 \cdot 10^{22}$	QRPA	[24]	1996
	$7.5 \cdot 10^{21}$	MCM-QRPA	[25]	1996
	$(1.0 - 3.1) \cdot 10^{23}$	RQRPA	[26]	1997
	$(1.2 - 5.8) \cdot 10^{23}$	RQRPA	[11]	2014
	$6.4 \cdot 10^{24}$	IBM-2	[14, 15]	2014
	$(2.3 - 6.7) \cdot 10^{24}$	SM	[16]	2014
$0_{\text{g.s.}}^+ - 2_2^+$ (1216.1 keV)	$> 1.4 \cdot 10^{21}$ (90 % C.L.)	exp.	[20]	1995
	$1.0 \cdot 10^{29}$	QRPA	[23]	1994
	$1.3 \cdot 10^{29}$	MCM-QRPA	[25]	1996
	$(0.7 - 2.2) \cdot 10^{28}$	RQRPA	[26]	1997

where the de-excitation  $\gamma$  ray is detected. This is achieved by searching for a  $\gamma$  ray of interest in one detector and labeling the other one as “source”. Note, that the distinction is made on the analysis level and that it might not be unique in some rare cases.

### 2.1. Event signature

The signatures of the investigated transitions are listed in the following (see also Fig. 1).

(i) The transition feeding the 559.1 keV level ( $0_{\text{g.s.}}^+ - 2_1^+$ ) has one single de-excitation  $\gamma$  ray of the same energy and thus a  $\beta\beta$  spectrum with 1480.0 keV endpoint energy.

(ii) The transition feeding the 1122.3 keV level ( $0_{\text{g.s.}}^+ - 0_1^+$ ) de-excites via the  $2_1^+$  state. A 563.2 keV  $\gamma$  ray is followed practically immediately by the 559.1 keV  $\gamma$  ray. The angular correlation  $W$  of the two  $\gamma$  rays in the  $0_1^+ - 2_1^+ - 0_{\text{g.s.}}^+$  cascade is given by

$W(\theta) \propto 1 - 3\cos^2\theta + 4\cos^4\theta$  where  $\theta$  is the angle between them [30]. The analysis searches for one of the two  $\gamma$  lines in the “gamma” detector. However, the energy resolution in GERDA does not allow to separate the two  $\gamma$  lines and a single peak region is used as region of interest. The  $\beta\beta$  endpoint energy is reduced to 916.8 keV.

(iii) The transition to 1216.1 keV level ( $0_{\text{g.s.}}^+ - 2_2^+$ ) has two decay branches: branch 1 with two de-excitation  $\gamma$  rays via the  $2_1^+$  state with energies of 657.0 keV and 559.1 keV. Branch 2 has a single de-excitation  $\gamma$  ray of 1216.1 keV directly into the ground state. The former has a branching ratio of 64 % leading to 36 % for branch 2. The angular correlation  $W$  of the two  $\gamma$  rays in the  $2_2^+ - 2_1^+ - 0_{\text{g.s.}}^+$  cascade of branch 1 is  $W(\theta) \propto 1 - \frac{15}{13}\cos^2\theta + \frac{16}{13}\cos^4\theta$ . The  $\beta\beta$  endpoint is reduced to 822.0 keV. The two branches are treated separately in the analysis and are later combined into a single value for the half-life.

## 2.2. The GERDA experiment

The GERmanium Detector Array (GERDA) is an experiment designed to investigate neutrinoless double beta decay of  $^{76}\text{Ge}$  with an array of high purity germanium (HPGe) detectors made from material with the  $^{76}\text{Ge}$  fraction enriched to  $\sim 87\%$ . The detectors are operated within a cryostat containing  $64\text{ m}^3$  of liquid argon (LAr) at the Laboratori Nazionali del Gran Sasso (LNGS) of Istituto Nazionale di Fisica Nucleare (INFN). The installation of the HPGe detectors in a closely spaced array with little material between the detectors facilitates an anti-coincidence veto for the  $0\nu\beta\beta$  search into the ground state suppressing  $\gamma$  ray background.

The GERDA setup is described in detail in Ref. [31]. The array of HPGe detectors used in Phase I of the experiment was organized into 4 strings of 3 to 5 detectors each. Three different detector types were used: semi-coaxial and BEGe detectors enriched in  $^{76}\text{Ge}$  ( $^{\text{enr}}\text{Ge}$ ) and semi-coaxial detectors with natural abundance ( $^{\text{nat}}\text{Ge}$ ). Five  $^{\text{enr}}\text{Ge}$  semi-coaxial detectors are from the Heidelberg-Moscow experiment [32], three  $^{\text{enr}}\text{Ge}$  semi-coaxial detectors from the IGEX experiment [33], and three  $^{\text{nat}}\text{Ge}$  semi-coaxial detectors from the GENIUS test facility [34]. All were refurbished for their operation in LAr. Additionally, an initial batch of five  $^{\text{enr}}\text{Ge}$  BEGe detectors produced for GERDA were employed [35]. The detector strings were lowered into LAr by a two-arm lock system supporting one string in one arm and three strings in the other [31].

## 2.3. Data sets and energy calibrations

The data of GERDA Phase I are used in this analysis. As described in Ref. [36], some detectors were removed and replaced by the 5 BEGe detectors after an initial data taking period. A higher background was observed for 49 d due to this change (silver data set as defined in Ref. [37]). For the present analysis this higher background period is omitted. The periods before and after had different detector array configurations and are treated independently in the analysis.

The data set is composed of runs of approximately 1 month each. Each selected run shows a stable operation of the whole array [37]. In some runs, individual detectors are excluded from the analysis due to temporary instabilities. In the present analysis every detector - also if its data is not used - is considered as source of the decay. A two-detector coincidence may be registered also in case the decay occurs in an excluded detector and the two  $\gamma$  rays are deposited in two active detectors. The efficiency calculation is taking these possibilities properly into account.

In the analysis, the target mass is defined as constant within each array configuration; changes due to inactive detectors are condensed into the signal detection efficiency of the array. The live-time sums up to an exposure of  $\mathcal{E}=31.04\text{ kg}\cdot\text{yr}$  for the whole data set including all  $^{\text{nat}}\text{Ge}$  and  $^{\text{emr}}\text{Ge}$  detectors. The isotopic exposure of  $^{76}\text{Ge}$  is  $\mathcal{E}_{76}=22.3\text{ kg}\cdot\text{yr}$ .

The same energy software-threshold of 100 keV is applied to all detectors. This basic threshold was applied to ensure a full reconstruction efficiency for all detector energies. After additional quality cuts and a  $\mu$ -veto cut the data set contains 2710 two-detector events and 82 three-detector events. This can be compared with  $\approx 7 \cdot 10^5$  single-detector events. The efficiency to detect de-excitation  $\gamma$  rays in three-detector events is more than one order of magnitude smaller and thus only two-detector events are further analyzed.

Energy calibrations were performed with  $^{228}\text{Th}$  sources typically once per week. In case of an energy deposition in more than one detector, cross-talk affects the reconstructed energy. Data taken by dedicated calibrations and the  $^{42}\text{K}$   $\gamma$  line in the physics data allow to measure the effect and hence to correct for it. The energy dependence of the cross-talk is linear in good approximation. The exposure averaged energy resolution (FWHM) of the 583 keV  $\gamma$  line from  $^{208}\text{Tl}$  is 4.2 keV for coincident events while it is 3.8 keV for events with energy deposition in one detector only. The uncertainty on the resolution is estimated to be 10 %.

#### 2.4. Monte Carlo simulations

Monte Carlo (MC) simulations were used to construct a specific background model for coincidence events and to determine the detection efficiencies. The background model described in Ref. [37] is used as a starting point where to additional background contributions had been added. Due to the coincidence requirement the individual background contributions to the spectra are of different significance when compared to the single-detector spectrum. Therefore, the evaluation of the background sources was tuned specifically for two-detector events. The main sources of background are contributions from  $^{214}\text{Bi}$ ,  $^{212}\text{Bi}$ ,  $^{208}\text{Tl}$ ,  $^{228}\text{Ac}$ ,  $^{40}\text{K}$  and  $^{60}\text{Co}$  on the detector holders,  $^{42}\text{K}$  and  $^{39}\text{Ar}$  distributed homogeneously in the LAr,  $^{42}\text{K}$  on the detector  $n^+$  contact and  $^{214}\text{Bi}$  on the detector  $p^+$  contact. Additionally, one further background contribution from  $^{108m}\text{Ag}$  in the signal cables was considered which is not part of the minimal background model in Ref. [37] and only visible in coincidence data.



The energy spectra from the data obtained with all the detectors and from the background model are shown in Fig. 2 for two-detector events. This background description is used for the development of cuts and the calculation of sensitivities but it does not enter itself in the final analysis. The left panel of Fig. 2 shows the individual detector energies in which each of the two detectors has a separate entry. The right panel shows the sum-energy spectrum; i.e., the total energy deposited in the array for a two-detector event. The shaded histograms show the data which can be directly compared to the background model shown in black. The individual background components for the semi-coaxial detectors only are shown in color; due to low statistics the ones for the BEGe detectors are omitted in the plot for clarity.

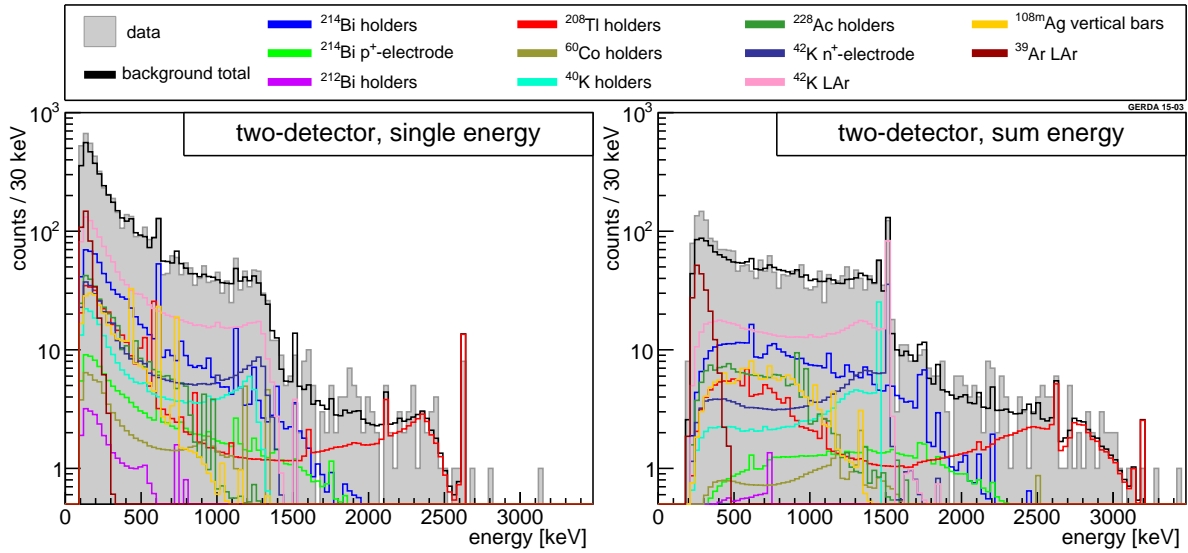


**Figure 2.** Data and background model for two-detector events after an individual detector threshold of 100 keV before cut optimization. In the single-energy spectra (left) each detector has a separate entry per event in the histogram whereas in the sum-energy spectra (right) the two energies are summed before histogramming. Data events are shown in solid gray and the background components for the coaxial detectors by the colored lines.

There are some differences found between background MC and data.

At low energy beta decay events from  $^{39}\text{Ar}$  with end point energy 565 keV dominate. The detected energy is highly sensitive to the exact knowledge of the detector dead layer which is not available. Hence data and Monte Carlo disagree here. The probability of a two-detector coincidence due to  $^{39}\text{Ar}$  is small and highly sensitive to the exact thickness of the detectors' dead layer. However, this effect is not relevant for the energy regions investigated in this analysis. Another excess is visible around 1.8 MeV in the single-energy spectrum in the data. However, it can not be due to a missing  $\gamma$  line or beta spectrum in the background model and furthermore the excess is not very significant. The agreement between the model and the data is sufficient for this analysis since the former is only used for cut optimization [38].



MC simulations were used to determine the signal efficiency for each decay mode. The simulations were performed with MAGE [39] which considers the angular correlation between the de-excitation  $\gamma$  rays. The detectors that were inactive in a given run are also set as inactive in the post-processing of the MC data. Each detector pair in each run has an individual signal detection efficiency which is then life-time weighted into a single number for the whole data set.

### 3. Analysis

The analysis is based on event counting in a region of interest (ROI) after a sequence of cuts. This is not a blind analysis, but special care was taken to avoid biases. The construction of the sequence of cuts starts with initial choices that are then optimized to maximize sensitivity. This aims to prevent *ad hoc* choices of analysis parameters. The MC background model and efficiency are used for the cut optimization. Systematic uncertainties and potential deficiencies in the background model only affect the choice of analysis parameters and do not have a direct effect on the derived half-life results since the background in the ROI is estimated from side bands (SB).

The spectra of the simulated  $2\nu\beta\beta$  decays scaled to  $10^{23}$  yr half-life are shown in Fig. 3. Also shown is the corresponding background model. The single-energy spectra and the sum-energy spectra are shown separately. The  $2\nu\beta\beta$  decays have a continuous shape in the sum-energy spectra due to the continuous electron component that is almost always detected in the source detector. The single-energy spectra show distinct de-excitation  $\gamma$  lines being detected outside the source detector enabling strong background reduction.

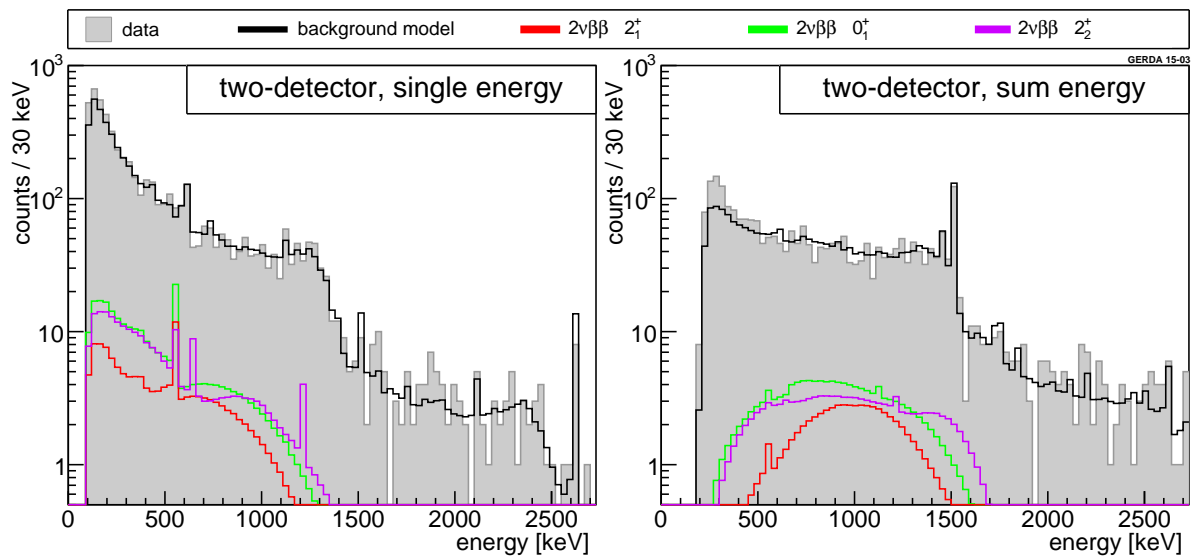


**Figure 3.** Illustration of the  $2\nu\beta\beta$  decays for two-detector events scaled to a half-life of  $10^{23}$  yr for each decay mode. Shown are the single-energy spectra (left) and the sum-energy spectra (right) before cut optimization. Also shown are the background model (black line) and data (gray histogram).

The energy distributions of two-detector coincidence events are shown in scatter plots (Fig. 4) for the simulated  $0_{\text{g.s.}}^+ - 0_1^+$  transition, the background model and the data. The color scale denotes the expected event densities for an excited state half-life of  $10^{23}$  yr and for the expected number of background events in the data set, respectively. The black points are data events. In this representation, horizontal and vertical lines are features of the single-energy spectra whereas diagonal lines are features of the sum-energy spectra. Many high energy background  $\gamma$  lines originate from outside the germanium detectors and can scatter into two detectors. These events can be suppressed with a cut on the sum energy. In Fig. 4 the diagonal  $\gamma$  line from  $^{42}\text{K}$  is clearly visible in the data and the background model. Additional  $\gamma$  lines from  $^{208}\text{Tl}$ ,  $^{40}\text{K}$  and  $^{214}\text{Bi}$  are only visible in the projections (see Figs. 2).

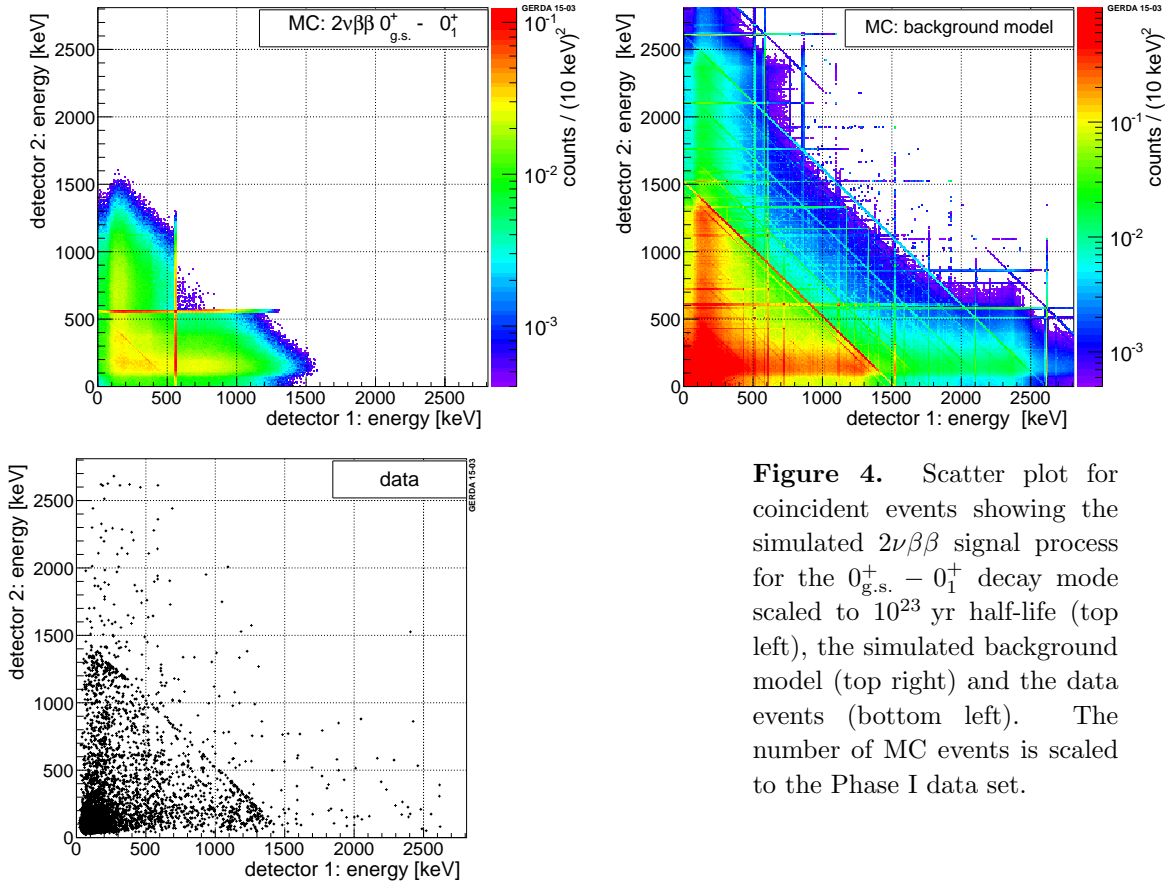


**Figure 4.** Scatter plot for coincident events showing the simulated  $2\nu\beta\beta$  signal process for the  $0_{\text{g.s.}}^+ - 0_1^+$  decay mode scaled to  $10^{23}$  yr half-life (top left), the simulated background model (top right) and the data events (bottom left). The number of MC events is scaled to the Phase I data set.

### 3.1. Sequence of cuts

A sequence of four cuts is applied:

1. **standard cuts:** quality cuts and  $\mu$  veto as in GERDA Phase I
2. **coincidence cuts:** specific two-detector cuts optimized for each decay mode
3. **background cuts:** exclusion of background  $\gamma$  lines

4. **detector pair cuts:** cuts to select detector pairs that exhibit a high efficiency

The cuts are designed to optimize the sensitivity  $\widehat{T}_{1/2}$ , expressed by the figure of merit  $S = \epsilon/\sqrt{B}$  with the signal detection efficiency  $\epsilon$  and the number of surviving background events  $B$ . The efficiency and the background in the sensitivity study are entirely based on MC simulations [40].

The **standard cuts** include quality cuts and the muon veto cut and are initially applied to the data set. They are identical to the cuts in the GERDA  $0\nu\beta\beta$  analysis (without pulse shape cuts) which are described in Ref. [36] and references therein.

The **coincidence cuts** are specific for each decay mode. They require a coincident event with either of the two detectors having the full energy of any de-excitation  $\gamma$  ray within a peak (energy) window size (PWS) of  $\pm 2\sigma_E$  where  $\sigma_E$  denotes the energy resolution at energy  $E$ . The PWS defines the specific ROI and SBs. Furthermore, a sum energy limit of 2039 keV is applied to exclude events with a total energy deposition larger than the possible energy release in  $^{76}\text{Ge}$ .

SBs are created by shifting the energy window of the coincidence cuts to lower and higher energies. The window size of a single SB is the same as for the corresponding ROI. To reduce the statistical uncertainty in the background estimation, a total of 4 SBs are defined for each decay mode; two at lower energies and two at higher energies. Based on the MC background model the SB regions are chosen for each decay mode individually. They are as close as possible to the ROI and avoid background  $\gamma$  lines in the single-energy spectra.

For two-detector events it is possible that the same event is tagged in the ROI and in a SB. A signal event that is tagged in the ROI has a 4% chance to be tagged also in one of the SBs. A background event in a SB has a 2% chance to be tagged also in another SB or the ROI. Events that are tagged in more than one of these five regions are rejected to avoid double counting in the statistical analysis. This reduces the signal efficiency by 4% and the background by 2% [40]. One event in the ROI of  $0_{\text{g.s.}}^+ - 2_2^+$  is removed by this requirement.

The **background cuts** are motivated by background  $\gamma$  lines that interfere with the ROIs. Fig. 5 shows the simulated sum-energy spectrum of the background model and the signal process after the coincidence cut for the  $0_{\text{g.s.}}^+ - 0_1^+$  transition. The low side cutoff is created by the smallest  $\gamma$  ray energy of interest (559.1 keV) in one detector and the single detector threshold of 100 keV in the other. The high cutoff is given by the sum energy limit. The dips in the spectra are created by rejecting events that are tagged in the ROI and a SB or two SBs simultaneously. The peak at 1122.3 keV for the signal process (green) is created by decays that occur in the dead layer of a detector or inside an excluded detector. In this case the  $\beta$  energy of the event is not detected and the two  $\gamma$  rays trigger a two-detector event with discrete sum energy.

The strongest peaks in the background spectrum (black line in Fig. 5) are found at 1524.7 keV and 1460.8 keV belonging to  $^{42}\text{K}$  and  $^{40}\text{K}$ , respectively. They represent the region in the scatter plot (Fig. 4, bottom) where the diagonal sum energy  $\gamma$  lines cross the

horizontal and vertical single energy lines of the  $2\nu\beta\beta$  decay. The next strongest feature in the background model is the peak around 1170 keV which is a combined structure: Firstly, a 609.3 keV  $^{214}\text{Bi}$   $\gamma$  ray coincides with another  $^{214}\text{Bi}$   $\gamma$  ray that scatters and deposits energy around the ROI of 559.1 keV in one detector; the 609.3 keV  $\gamma$  ray is fully detected in the other detector creating a sum energy around 1170 keV. Secondly, a similar coincidence with a 614.3 keV  $^{108m}\text{Ag}$   $\gamma$  ray and another one from the  $^{108m}\text{Ag}$  decay can happen. The other peaks originate mainly from  $^{214}\text{Bi}$ ,  $^{228}\text{Ac}$  or  $^{60}\text{Co}$ . They are created either (1) by a single  $\gamma$  ray scattering into two detectors or (2) by two  $\gamma$  rays with one  $\gamma$  ray fully detected in one detector. In both cases an energy around  $\approx 560$  keV has to be deposited in at least one detector. This can be identified in Fig. 4 where the horizontal/vertical cut window crosses anti-diagonal background lines in scenario (1) or horizontal/vertical background lines in scenario (2).

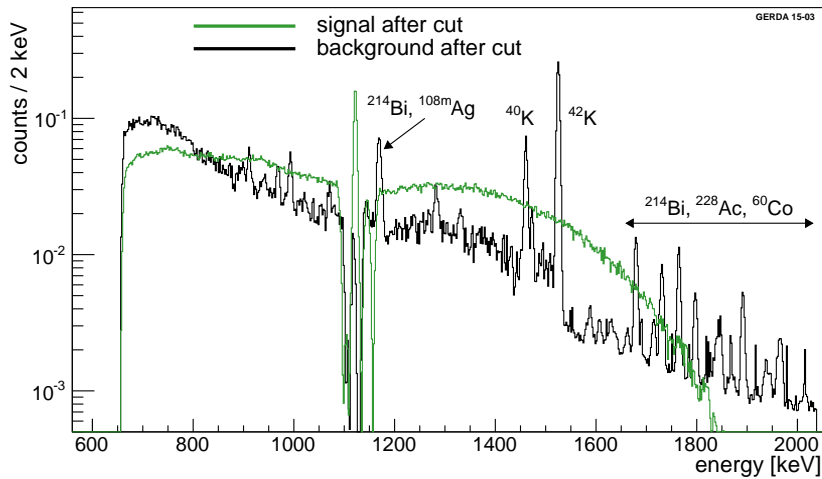


**Figure 5.** Simulated sum-energy spectrum after coincidence cuts for the  $0_{\text{g.s.}}^+ - 0_1^+$  transition. The background model (black) and signal process scaled to  $10^{23}$  yr half-life (green) are shown.

The background cuts are applied to all decay modes in the same way.  $^{42}\text{K}$  and  $^{40}\text{K}$  are excluded by requiring the detector sum energy not to be in the range of  $1524.7 \pm 5.5$  keV nor in  $1460.8 \pm 5.4$  keV. The energy ranges correspond to  $2\sigma_E$ . Additionally, the individual detector energy is required to be outside  $611.0 \pm 5.7$  keV to exclude the  $^{214}\text{Bi}$  and  $^{108m}\text{Ag}$  background.

At this stage, the combination of coincidence cuts and background cuts can be optimized in three ways. The individual detector threshold is scanned from 100 keV to 500 keV in steps of 50 keV. This is equivalent of increasing the low energy cutoff in Fig. 5. The figure of merit  $S$  is determined for each step and the individual detector threshold with the highest  $S$  is chosen as the optimized cut. In a similar way the sum energy limit is scanned from 1000 keV to  $Q_{\beta\beta}$  in steps of 50 keV. This is equivalent of changing the high energy cutoff in Fig. 5. Finally also the peak window size is scanned from  $1\sigma$  to  $2\sigma$  energy resolution in steps of 0.2 keV. The optimization of these cut parameters is performed individually for all three decay modes. The optimal values are

shown in Table 2 along with their relative sensitivity gain compared to the base values.

**Table 2.** Optimized values for individual detector threshold (IDT), sum energy limit (SEL) and the peak window size (PWS). The respective ROIs are given as absolute ranges; the \* indicates an expanded range due the occurrence of more than one  $\gamma$  line. The sensitivity gain is related to the base values before background cuts.

mode	IDT [keV]	SEL [keV]	PWS [keV]	size ROI [keV]	sensitivity gain [ %]
$0_{\text{g.s.}}^+ - 2_1^+$	450	1750	$\pm 2.6$	[556.5 – 561.7]	41.3
$0_{\text{g.s.}}^+ - 0_1^+$	250	1750	$\pm 2.2$	[556.9 – 565.4]*	18.9
$0_{\text{g.s.}}^+ - 2_2^+$ B1	250	1800	$\pm 2.4$	[556.7 – 561.5]	20.4
			$\pm 3.0$	$\vee$ [654.0 – 660.0]*	
$0_{\text{g.s.}}^+ - 2_2^+$ B2	300	1850	$\pm 2.8$	[1213.3 – 1218.9]	98.5
base values	100	2039	$2\sigma_E$		

The **detector pairs** of coincidence events which are used in the analysis are also tuned to maximize  $S$ . Each detector pair is composed of the gamma detector and the source detector which are identified by containing the energy deposition in the ROI or an arbitrary energy deposition within the allowed energy range, respectively. This results in an asymmetric effect for  $^{\text{nat}}\text{Ge}$  and  $^{\text{enr}}\text{Ge}$  detectors:  $^{\text{enr}}\text{Ge}$  detectors are more likely to be the source of a  $2\nu\beta\beta$  decay than  $^{\text{nat}}\text{Ge}$  detectors but have an equal chance to detect  $\gamma$  rays. Taking into account all data sets there are in total 28 detector pairs in the GERDA array and 56 detector pairs if the distinction between source detector and gamma detector is taken into account. The maximization of  $S$  selects 37 pairs. The sensitivity gain from the pair selection is between 7 and 10 % depending on the decay mode. More detailed information on the sequence of cuts are reported in Ref. [40].

After applying the full sequence of cuts, the validity of the SB regions is tested. For these regions a flat background is required. In case the SBs are symmetrically placed around the ROI, also a linear background is sufficient. Table 3 shows the expected and the observed event count for each SB. For the  $2_1^+$  mode the model predicts a flat background while for the others the expected counts at higher energies (SB4) is slightly smaller. However the average agrees with the background model prediction in the ROI. This validates the SBs to be used as background estimators for the ROI.

## 4. Results

The single-energy spectra around the respective ROI are shown in Fig. 6 for all decay modes. All two-detector coincident events with decay mode optimized individual detector threshold and sum energy limit are shown in light gray; no other cuts are applied. The corresponding MC background model is shown in black for illustration. Events passing all cuts have exactly one entry in one of the 5 intervals (but two entries

**Table 3.** Summary of SBs after the complete sequence of cuts for each decay mode. Listed are the relative position  $\Delta E$  of the four SBs compared to the ROI, the number of events  $N_{\text{MC}}$  in the MC background model and the number of events  $N_{\text{data}}$  in the data set. Additionally the background expectations in the ROI and the observed events are shown after application of all cuts. The uncertainty of the MC expectations denote statistical uncertainties only.

Region	$\Delta E$	$N_{\text{MC}}$	$N_{\text{data}}$	Region	$\Delta E$	$N_{\text{MC}}$	$N_{\text{data}}$
$0_{\text{g.s.}}^+ - 2_1^+$ 559.1 keV				$0_{\text{g.s.}}^+ - 0_1^+$ 559.1 & 563.2 keV			
SB 1	-7.5 keV	$2.5 \pm 0.1$	2	SB 1	-12 keV	$8.0 \pm 0.1$	7
SB 2	+7.5 keV	$2.4 \pm 0.1$	0	SB 2	+12 keV	$7.5 \pm 0.1$	11
SB 3	-15 keV	$2.6 \pm 0.1$	3	SB 3	-24 keV	$8.3 \pm 0.1$	7
SB 4	+15 keV	$2.4 \pm 0.1$	5	SB 4	+35 keV	$6.8 \pm 0.1$	9
average SB		$2.5 \pm 0.1$	2.5	average SB		$7.7 \pm 0.1$	8.5
ROI		$2.5 \pm 0.1$	2	ROI		$7.9 \pm 0.1$	5
$0_{\text{g.s.}}^+ - 2_2^+$ branch 1: 559.1 & 657.0 keV				$0_{\text{g.s.}}^+ - 2_2^+$ branch 2: 1216.1 keV			
SB 1	-8 keV	$8.5 \pm 0.1$	6	SB 1	-19 keV	$0.52 \pm 0.02$	1
SB 2	+18 keV	$8.1 \pm 0.1$	5	SB 2	+10 keV	$0.39 \pm 0.02$	0
SB 3	-16 keV	$8.7 \pm 0.1$	6	SB 3	-27 keV	$0.58 \pm 0.02$	0
SB 4	+35 keV	$7.9 \pm 0.1$	12	SB 4	+47 keV	$0.32 \pm 0.02$	1
average SB		$8.3 \pm 0.1$	7.25	average SB		$0.45 \pm 0.01$	0.5
ROI		$8.3 \pm 0.1$	6	ROI		$0.40 \pm 0.02$	0

in the single-energy spectrum). The ones in the ROI are shown in red and the ones of the SBs in blue.

Frequentist 90 % confidence level and Bayesian 90 % credibility lower values were calculated for  $T_{1/2}$ . The Frequentist values were based on a bounded profile likelihood test statistic [41] increased by 2.7 compared to the minimum. It was verified that this method has always sufficiency coverage. For the Bayesian credibility limit, a flat prior in  $T_{1/2}^{-1}$  was assumed as well as a flat prior in the background level.

In both approaches the same likelihood was used which is constructed for the inverse half-life  $T_{1/2}^{-1}$ . In case of two decay branches as for  $2\nu\beta\beta$   $0_{\text{g.s.}}^+ - 2_2^+$ , the likelihood is treated as two individual data sets with a common  $T_{1/2}^{-1}$ . The expectation for the signal counts for a given decay branch ( $k$ ) is:

$$s_k = \ln 2 \cdot \eta_k \cdot \mathcal{E} \cdot T_{1/2}^{-1}, \quad (3)$$

with the decay branch specific efficiency  $\eta_k$ . The efficiency is the live-time weighted averaged detection efficiency of a  $2\nu\beta\beta$  decay excited state event over all runs in the two array configurations of GERDA Phase I. The exposure  $\mathcal{E}$  is defined as the combined total isotopic exposure for  $^{76}\text{Ge}$  in the data set for all detectors. The expected number

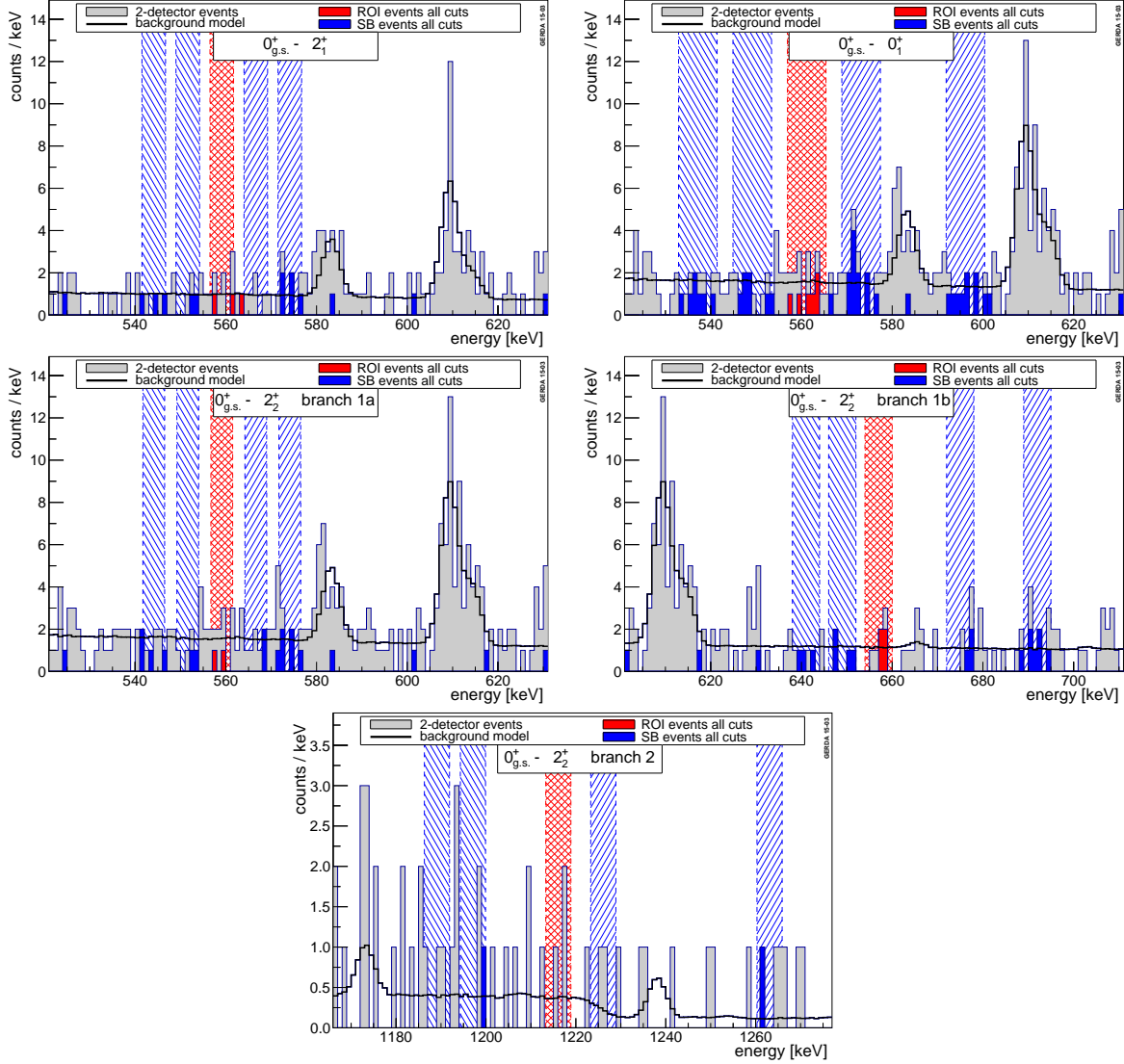


**Figure 6.** Single-energy spectra around the respective ROI for all decay modes. Shown are all two-detector events for the optimized individual detector threshold and sum energy limit (light gray) and the corresponding background curves (black). The optimized cuts result in different two-detector spectra for each decay mode. Also shown are the ROI (shaded red) and SB region (shaded blue). Highlighted are events that are tagged as ROI (red) and SB (blue) after all cuts and that are used for the limit setting. Note that the histograms contain two entries per event and that one entry may lie outside the tagging region.

of events in the ROI is:

$$\mu_k = \frac{b_k}{4} + s_k \quad (4)$$

using the total background from all 4 SBs  $b_k$ .

The full expression of the likelihood is constructed with three terms: (1) a Poisson term describing the probability of signal plus background in the ROI, (2) a Poisson penalty term accounting for the uncertainty of the background level in the ROI and (3)



a Gaussian penalty term accounting for all systematic uncertainties condensed into the efficiency. The likelihood depends on  $T_{1/2}^{-1}$ , the number of counts in the ROI ( $n_k$ ), the number of counts in all SBs ( $m_k$ ) and the efficiency expectation ( $\epsilon_k$ ):

$$\begin{aligned} \mathcal{L} & \left( n_k, m_k, \epsilon_k | T_{1/2}^{-1}, b_k, \eta_k \right) \\ & = \prod_k \left[ \frac{(\mu_k)^{(n_k)}}{(n_k)!} \cdot e^{-\mu_k} \right] \cdot \left[ \frac{(b_k)^{(m_k)}}{(m_k)!} \cdot e^{-b_k} \right] \cdot \left[ \frac{1}{\sigma_{\epsilon_k} \sqrt{2\pi}} \cdot e^{-\frac{1}{2} \left( \frac{\epsilon_k - \eta_k}{\sigma_{\epsilon_k}} \right)^2} \right]. \end{aligned} \quad (5)$$

For the profile likelihood we calculate  $-2 \log \mathcal{L}$ . In the extraction of the posterior probability [42], flat priors for all fit parameters  $T_{1/2}^{-1}$ ,  $b_k$  and  $\eta_k$  were used since the prior information on the background and efficiency is included in the likelihood with penalty terms.

Systematic uncertainties on the signal efficiency are estimated with MC simulations and combined into a single value  $\sigma_{\epsilon_k}$  assuming no correlations. The sources of these uncertainties are the active volume and dead layer thicknesses of the detectors (5%), the energy resolution and energy shift after cross talk correction (3%), the MC simulations (4%) and the uncertainty on the isotopic abundance (2.5%), where the numbers in parentheses give the resulting uncertainty on the signal efficiency. The combined relative systematic uncertainty on the efficiency is 7.5% for all decay modes. The systematic uncertainty was investigated for the  $0_{\text{g.s.}}^+ - 0_1^+$  transition and assumed to be similar for all decay modes.

A sensitivity study was performed using a toy MC under the assumption of no signal. The inverse half-life limit was calculated  $10^4$  times with randomly changing input parameters;  $n_k^{\text{rand}}$  and  $m_k^{\text{rand}}$  were each randomized according to a Poisson distribution. The expectation values of this distribution were taken from the background model prediction  $N_{\text{MC}}$  and  $4 N_{\text{MC}}$ , respectively (Table 3).  $\epsilon_k^{\text{rand}}$  is randomized with a Gaussian distribution with a mean of  $\epsilon_k$  and a width of  $\sigma_{\epsilon_k}$ . The median of the 90% quantile inverse half-life limit distribution is taken as the sensitivity.

Table 4 shows the input parameter for the statistical analysis ( $n_k$ ,  $m_k$  and  $\epsilon_k$ ) in the first 3 columns. The next two columns show the Frequentist 90% C.L. lower value for  $T_{1/2}$  and the expected sensitivity  $\widehat{T}_{1/2}$  from the toy MC study. The last two columns show the Bayesian 90% credibility lower bound on  $T_{1/2}$  and the respective sensitivity  $\widehat{T}_{1/2}$ .

*decay mode  $2\nu\beta\beta$   $0_{\text{g.s.}}^+ - 2_1^+$ :* The transition to the excited  $2_1^+$  has one 559.1 keV de-excitation  $\gamma$  ray and hence a small coincidence efficiency compared to the other excited state decay modes. After all cuts 2 events are observed in the ROI and 2.5 events are expected from the side bands. No signal is found and the Frequentist analysis yields a 90% lower value on the half-life:  $T_{1/2}^{2\nu} > 1.6 \cdot 10^{23}$  yr. The sensitivity as defined above is  $1.3 \cdot 10^{23}$  yr. The Bayesian analysis yields lower credibility bounds on the half-life of  $T_{1/2}^{2\nu} > 1.3 \cdot 10^{23}$  yr (90% C.I.) with a sensitivity of  $1.2 \cdot 10^{23}$  yr.

**Table 4.** Summary of results for all decay modes. Shown from left to right are the input parameters for the likelihood:  $n$  - number of events within the ROI,  $m$  - number of events with in SB(1-4),  $\epsilon$  - detection efficiency. The following columns show the Frequentist lower half-life limit and the sensitivity which contains the true value in 90% of the cases. The last two columns show the Bayesian lower limit for half-life values with more than 90% probability and the respective sensitivity.

Decay mode	$n_k$	$m_k$	$\epsilon_k$ [%]	Frequentist 90% C.L.		Bayesian 90% C.I.	
				$T_{1/2}$ [ $10^{23}$ yr]	$\widehat{T}_{1/2}$ [ $10^{23}$ yr]	$T_{1/2}$ [ $10^{23}$ yr]	$\widehat{T}_{1/2}$ [ $10^{23}$ yr]
$0_{\text{g.s.}}^+ - 2_1^+$	2	10	0.389	> 1.6	> 1.3	> 1.3	> 1.2
$0_{\text{g.s.}}^+ - 0_1^+$	5	34	0.919	> 3.7	> 1.9	> 2.7	> 1.8
$0_{\text{g.s.}}^+ - 2_2^+$ branch 1	6	29	0.594	> 1.7	> 1.2	> 1.4	> 1.1
$0_{\text{g.s.}}^+ - 2_2^+$ branch 2	0	2	0.092	> 0.74	> 0.64	> 0.49	> 0.46
$0_{\text{g.s.}}^+ - 2_2^+$ combined	-	-	-	> 2.3	> 1.4	> 1.8	> 1.3

This lower half-life limit for the  $2\nu\beta\beta$   $0_{\text{g.s.}}^+ - 2_1^+$  transition is two orders of magnitude better than previous best limits. However, the current theoretical prediction are beyond the experimental reach. The most recent calculation [28] predicts a half-life longer by 4 orders of magnitude. The lowest half-life prediction by the Hartree-Fock-Bogoliubov approach is still a factor of 6 above the current sensitivity. The largest half-life prediction by shell model calculations is even 7 orders of magnitude above the current limit.

*decay mode  $2\nu\beta\beta$   $0_{\text{g.s.}}^+ - 0_1^+$ :* The transition to the excited  $0_1^+$  state has two de-excitation  $\gamma$  rays of 559.1 keV and 563.2 keV in the final state and the largest efficiency of the considered decay modes. It also has the lowest theoretically predicted half-life and is thus of special interest. After all cuts, 8.5 events are expected in the ROI and 5 events are observed. No signal is found; a lower half-life value of  $3.7 \cdot 10^{23}$  yr (90% C.L.) is set for the Frequentist analysis and  $2.7 \cdot 10^{23}$  yr (90% C.I.) for the Bayesian analysis. The sensitivities are  $1.9 \cdot 10^{23}$  yr and  $1.8 \cdot 10^{23}$  yr, respectively.

This lower half-life limit is 2.5 orders of magnitude better than previous results for the  $2\nu\beta\beta$   $0_{\text{g.s.}}^+ - 0_1^+$  transition. The new limit is well within the region of theoretical predictions. Bayes factors are calculated for testing the hypothesis of each NME model in Table 1 by taking the ratio  $B = p(H_1)/p(H_0)$  in which  $H_1$  is the NME model hypothesis with  $T_{1/2}^{\text{Model}}$  and  $H_0$  the hypothesis of only background. The models in Refs. [22, 23, 24, 25] have  $B < 10^{-6}$  and are ruled out. The QRPA model [26] has  $B = 0.001 - 0.19$  for  $T_{1/2} = (1.0 - 3.1) \cdot 10^{23}$  yr, respectively. Recent calculations with RQRPA [11], IBM-2 [14] and SM [16] predict significantly longer half-lives. For RQRPA a range can be constrained:  $B = 0.005$  for  $g_A = 1.00$  ( $T_{1/2} = 1.2 \cdot 10^{23}$  yr) compared to  $B = 0.45$  for  $g_A = 1.26$  ( $T_{1/2} = 5.8 \cdot 10^{23}$  yr). The IBM-2 and SM prediction are still above the current experimental reach.

*decay mode  $2\nu\beta\beta$   $0_{\text{g.s.}}^+ - 2_2^+$ :* The transition into the excited  $2_2^+$  state has two de-excitation branches: Branch 1 (64% probability) with two  $\gamma$  ray emissions of 559.1 keV and 657.0 keV and branch 2 (36% probability) with a single  $\gamma$  ray emission of 1216.1 keV. Branch 1 shows a significantly larger efficiency due to the higher branching ratio; on the other hand, the ROI for branch 2 is at higher energy resulting in lower background level. 7.25 events are expected and 6 events are observed for branch 1 compared to 0.5 expected and no observed event in branch 2. No signal is found in either branch and a combined limit is calculated according to Eq. 5 with  $k = 1, 2$ : The Frequentist 90% C.L. lower value is  $2.3 \cdot 10^{23}$  yr. The Bayesian analysis yields a 90% credibility lower bound of  $1.8 \cdot 10^{23}$  yr. The corresponding half-life sensitivities are  $1.4 \cdot 10^{23}$  yr and  $1.3 \cdot 10^{23}$  yr, respectively.

For the  $2\nu\beta\beta$   $2_{\text{g.s.}}^+ - 2_2^+$  transition the lower half-life limit was improved by 2 orders of magnitude compared to previous limits. The theoretical predictions for this transition are  $>10^{28}$  yr and cannot be tested with the current sensitivity.

## 5. Conclusions

An analysis for  $2\nu\beta\beta$  excited state transitions in  $^{76}\text{Ge}$  with the GERDA Phase I data set has been performed for the three decay modes  $0_{\text{g.s.}}^+ - 2_1^+$ ,  $0_{\text{g.s.}}^+ - 0_1^+$  and  $0_{\text{g.s.}}^+ - 2_2^+$ . The analysis is performed without blinding, however the automated choice of cuts is expected to have reduced bias: All cut parameters are chosen such that the sensitivity calculated from MC simulations is maximized. No signal has been found and new half-life lower limits are set for all decay modes which are at least two orders of magnitude larger than those reported previously. Bayes factors are calculated for the predictions of the  $0_{\text{g.s.}}^+ - 0_1^+$  half-life with various nuclear models. Many old NME calculations could be ruled out.

The analysis is based on the assumption that only one decay mode is realized at a time. This is valid in the present case for the non-observation of a signal. Hence, the analysis is performed on each decay mode completely independently. However, it should be noted that the results of the different decay modes are not decoupled since they proceed through the same levels. Particularly the 559.1 keV  $\gamma$  line of the  $0_{\text{g.s.}}^+ - 2_1^+$  transition is part of all decay modes. The Frequentist lower half-life limits are larger than the sensitivity in all cases. A statistical background downward fluctuation in the 559.1 keV region, as observed, has a similar influence on all limits. For additional information refer to a more detailed description of this analysis in Ref. [40].

In the future Phase II of the GERDA experiment it will be possible to increase the sensitivity further. The target mass of  $^{\text{enr}}\text{Ge}$  detectors will be increased by a factor of two in form of relatively small BEGes detectors. The overall background level is expected to be reduced by an order of magnitude.

## 6. Acknowledgments

The GERDA experiment is supported financially by the German Federal Ministry for Education and Research (BMBF), the German Research Foundation (DFG) via the Excellence Cluster Universe, the Italian Istituto Nazionale di Fisica Nucleare (INFN), the Max Planck Society (MPG), the Polish National Science Centre (NCN), the Russian Foundation for Basic Research (RFBR), and the Swiss National Science Foundation (SNF). The institutions acknowledge also internal financial support.

We greatly acknowledge and thank Jouni Suhonen, Francesco Iachello and Javier Menéndez for providing nuclear matrix element calculations for the investigated decay modes.

The GERDA collaboration thanks the directors and the staff of the LNGS for their continuous strong support of the GERDA experiment. Furthermore we acknowledge the use of the CPU farm ATLAS of ZIH at TU Dresden for extensive Monte Carlo simulations.

## References

- [1] Suhonen J and Civitarese O, 2012 J. Phys. G: Nucl. Part. Phys. **39** 124005.
- [2] Tretyak V and Zdesenko Y G, 2002 Atom. Data Nucl. Data Tabl. **80** 83.
- [3] Ackerman N *et al.* (EXO Collaboration), 2011 Phys. Rev. Lett. **107** 212501.
- [4] Avignone III F T, Elliott S R, and Engel J, 2008 Rev. Mod. Phys. **80** 1.
- [5] Barabash A S *et al.*, 1995 Phys. Lett. B **345** 408.
- [6] Barabash A S, Hubert F, Hubert P, and Umatov V I, 2004 JETP Lett. **79** 10.
- [7] Arnold R *et al.* (NEMO-3 Collaboration), 2014 Nucl. Phys. A **925** 25.
- [8] Barabash A, Hubert P, Nachab A, and Umatov V, 2009 Phys. Rev. C **794** 045501.
- [9] Mount B J, Redshaw M, and Myers E G, 2010 Phys. Rev. C **81** 032501.
- [10] Suhonen J, 2011 Nucl. Phys. A **853** 36.
- [11] Suhonen J, unpublished March 2014.
- [12] Barea J, Kotila J, and Iachello F, 2013 Phys. Rev. C **871** 014315.
- [13] Kotila J and Iachello F, 2012 Phys. Rev. C **853** 034316.
- [14] Iachello F, unpublished June 2014.
- [15] Agostini M *et al.* (GERDA Collaboration), 2015 arXiv:1501.02345.
- [16] Menéndez J, unpublished September 2014.
- [17] Menéndez J, Poves A, Caurier E, and Nowacki F, 2009 Nucl. Phys. A **8183-4** 139.
- [18] Caurier E, Nowacki F, and Poves A, 2012 Phys. Lett. B **7111** 62.
- [19] Beck M, *et al.* (Heidelberg-Moscow Collaboration), 1992 Z. Phys. A **343** 397.
- [20] Barabash A S, Derbin A V, and Popeko L A, 1995 Z. Phys. A **352** 231.
- [21] Haxton W. C and Stephenson Jr G. J, 1984 Prog. Part. Nucl. Phys. **12** 409.
- [22] Dhiman S and Raina P, 1994 Phys. Rev. C **50** R2660.
- [23] Civitarese O and Suhonen J, 1994 Nucl. Phys. A **575** 251.
- [24] Stoica S and Mihut I, 1996 Nucl. Phys. A **A6022** 197.
- [25] Aunola M and Suhonen J, 1996 Nucl. Phys. A **602** 133.
- [26] Toivanen J and Suhonen J, 1997 Phys. Rev. C **55** 2314.
- [27] Schwieger J, Šimkovic F, Faessler A, and Kamiński W, 1998 Phys. Rev. C **57** 1738.
- [28] Unlu S, 2014 Chin. Phys. Lett. **314** 042101–5.
- [29] Vasilev S I, Klimenko A A, Osetrov S B, and Smolnikov A A, 2000 JETP Lett. **72** 279.
- [30] Schatz G and Weidinger A, 1997 Nukleare Festkörperphysik, Teubner
- [31] Ackermann K *et al.* (GERDA Collaboration), 2013 Eur. Phys. J. C **73** 2330.
- [32] Klapdor-Kleingrothaus *et al.* H V, 2001 Eur. Phys. J. A **12** 147.
- [33] Aalseth C E *et al.* (IGEX Collaboration), 2002 Phys. Rev. D **659** 092007.

- [34] Klapdor-Kleingrothaus H V *et al.*, 2002 Nucl. Instr. Meth. A **4811-3** 149.
- [35] M. Agostini, *et al.*, (GERDA Collaboration), 2015 Eur. Phys. J. C **75** 39.
- [36] Agostini M *et al.* (GERDA Collaboration), 2013 Phys. Rev. Lett. **111** 122503.
- [37] Agostini M *et al.* (GERDA Collaboration), 2014 Eur. Phys. J. C **74** 2764.
- [38] Wester T, 2015 PhD thesis in preparation .
- [39] Boswell M *et al.*, 2011 IEEE Trans. Nucl. Sci. **583** 1212.
- [40] Lehnert B, 2015 PhD thesis to be published .
- [41] Rolke W A, López A M, and Conrad J, 2005 Nucl. Instr. Meth. A **5512-3** 493.
- [42] Caldwell A, Kollár D, and Kröninger K, 2009 Comp. Phys. Comm. **18011** 2197.